materials

MDPI

Article

Crystallisation Phenomena of In_2O_3:H Films

Ruslan Muydinov [1,*], Alexander Steigert [2], Markus Wollgarten [3], Paweł Piotr Michałowski [4], Ulrike Bloeck [3], Andreas Pflug [5], Darja Erfurt [6], Reiner Klenk [6], Stefan Körner [1], Iver Lauermann [6] and Bernd Szyszka [1]

1 Institute of High-Frequency and Semiconductor System Technologies, Technical University Berlin, Einsteinufer 25, 10587 Berlin, Germany; s.koerner@tu-berlin.de (S.K.); bernd.szyszka@tu-berlin.de (B.S.)
2 Institute for Nanospectroscopy, Helmholtz-Zentrum Berlin für Materialien und Energie GmbH, Albert-Einstein-Str. 15, 12489 Berlin, Germany; alexander.steigert@helmholtz-berlin.de
3 Department of Nanoscale Structures and Microscopic Analysis, Helmholtz-Zentrum Berlin für Materialien und Energie GmbH, Hahn-Meitner-Platz 1, 14109 Berlin, Germany; wollgarten@helmholtz-berlin.de (M.W.); bloeck@helmholtz-berlin.de (U.B.)
4 Institute of Electronic Materials Technology, Wolczynska Str. 133, 01919 Warsaw, Poland; Pawel.Michalowski@itme.edu.pl
5 Fraunhofer Institute for Surface Engineering and Thin Films IST, Bienroder Weg 54e, 38108 Braunschweig, Germany; Andreas.Pflug@ist.fraunhofer.de
6 PVcomB, Helmholtz-Zentrum Berlin für Materialien und Energie GmbH, Schwarzschildstr. 3, 12489 Berlin, Germany; darja.erfurt@helmholtz-berlin.de (D.E.); klenk@helmholtz-berlin.de (R.K.); iver.lauermann@helmholtz-berlin.de (I.L.)
* Correspondence: ruslan.muydinov@tu-berlin.de

Received: 21 November 2018; Accepted: 4 January 2019; Published: 15 January 2019

Abstract: The crystallisation of sputter-deposited, amorphous In_2O_3:H films was investigated. The influence of deposition and crystallisation parameters onto crystallinity and electron hall mobility was explored. Significant precipitation of metallic indium was discovered in the crystallised films by electron energy loss spectroscopy. Melting of metallic indium at ~160 °C was suggested to promote primary crystallisation of the amorphous In_2O_3:H films. The presence of hydroxyl was ascribed to be responsible for the recrystallization and grain growth accompanying the inter-grain In-O-In bounding. Metallic indium was suggested to provide an excess of free electrons in as-deposited In_2O_3 and In_2O_3:H films. According to the ultraviolet photoelectron spectroscopy, the work function of In_2O_3:H increased during crystallisation from 4 eV to 4.4 eV, which corresponds to the oxidation process. Furthermore, transparency simultaneously increased in the infraredspectral region. Water was queried to oxidise metallic indium in UHV at higher temperature as compared to oxygen in ambient air. Secondary ion mass-spectroscopy results revealed that the former process takes place mostly within the top ~50 nm. The optical band gap of In_2O_3:H increased by about 0.2 eV during annealing, indicating a doping effect. This was considered as a likely intra-grain phenomenon caused by both $(In^0)_O^{\bullet\bullet}$ and $(OH^-)_O^{\bullet}$ point defects. The inconsistencies in understanding of In_2O_3:H crystallisation, which existed in the literature so far, were considered and explained by the multiplicity and disequilibrium of the processes running simultaneously.

Keywords: In_2O_3:H; thin films; crystallisation; TCO; high mobility

1. Introduction

Hydrogen doped indium oxide (In_2O_3:H) films demonstrate an electron Hall mobility (μ_e) of over 100 cm^2/Vs [1,2]. Such outstanding property can be achieved if the In_2O_3 film is deposited in an amorphous state and subsequently crystallised at T > 160 °C. Its optical transmittance is superior

in both ultraviolet (UV) and near-infrared (NIR) spectral ranges when compared to the widely used transparent conductive oxides (TCOs), such as ZnO:Al or In_2O_3:Sn. This results in a performance gain for Si-based [3–5] and CIGS (Cu-In-Ga-S/Se)-based [6–8] solar cells.

Amorphous In_2O_3 films are usually obtained by sputter-deposition in the presence of water vapour without intentional heating [1,2]. Low crystallisation temperatures make them applicable on top of a-Si and CIGS-absorbers. Moreover, the crystallisation seems to proceed within a few minutes [3]. Thus In_2O_3:H can be essential for tandem solar cell concepts, e.g., with hybrid perovskites.

There is a number of thorough theoretical and experimental investigations on In_2O_3, its defectiveness and interaction with a gas phase. Nevertheless, some ambiguity with respect to the origin of the *n*-type conductivity, the role of the crystallisation and the origin of the high carrier mobility In_2O_3:H films still exists. For instance, there is no satisfactory explanation for the following phenomenon so far: the crystallisation of In_2O_3:H films is accompanied with a Burstein-Moss shift and a decrease of the charge carrier concentration (N_e) simultaneously. At the same time, it is widely accepted in literature that the *n*-type doping of crystalline In_2O_3 is related to the hydrogen incorporation. Another important disagreement concerns the "high mobility". Exactly the passivation of dangling bonds on grain-boundaries by hydrogen is supposed to be the most probable reason for high mobility [9]; however, only this intergranular hydrogen disappears primarily during heating in vacuum [10].

Our recent studies revealed the effect of oxygen addition to the sputter-gas on the In_2O_3:H crystallisation progress [11]. However, the question of whether we deal with so-called plasma damage still remains. This negative effect of the accelerated O^- ions largely determines electrical properties and their spatial deviations over the film [12,13].

The inconsistencies noted above represent a lack of understanding of the In_2O_3:H material. In this work we investigated microstructural, compositional, optical and electrical properties of the In_2O_3 and In_2O_3:H films. We also observed how these properties change during In_2O_3 crystallisation. Additionally, the discussion section contains a brief review of the relevant findings accumulated so far in literature. Finally, we attempted to compose a full puzzle from all these data and understand this material better.

2. Experimental Section

The as-deposited films will be further assigned as In_2O_3:H_2O, because they were found to contain hydroxyl groups. The post-deposition annealed films we denote by In_2O_3:H, as widely accepted. In_2O_3:H_2O films were obtained in a stationary mode by RF (Radio Frequency, 13.56 MHz) magnetron sputtering from a round Ø 3″ ceramic In_2O_3 (99.99%) target onto unheated, stationary 1″ × 1″ Eagle XG (Corning, 0.7 mm thick) glass substrates. The substrates were cleaned in a multistage glass-washer using surfactants and de-ionised water. The target-to-substrate distance was fixed at the optimum 40 mm. The RF power was set at 60 W, which results in 1.3 W/cm^2 power density. The base pressure of the sputtering system was 5×10^{-6} Pa. Water vapour was admitted through a needle valve from a reservoir. Adjusting the valve manually, the $p(H_2O)$ was stabilised at 2×10^{-3} Pa prior to the deposition. The sputtering gas was pure Ar, and the following process pressures were compared: 0.5 Pa (Ar flow: 20 sccm) and 1.3 Pa (Ar flow: 100 sccm). The films were annealed after deposition under different $p(O_2)$ conditions: ~21 kPa (ambient air) or ~10^{-6} Pa (ultra-high vacuum). Very thin (~20 nm) films obtained on 0.3 mm thick Si-wafers were analysed by XPS/UPS without breaking vacuum in the combined deposition and surface analysis system (CISSY) [14]. It includes a standard XPS laboratory module with a non-monochromatic X-ray source and Mg (Al) anodes providing an excitation energy of 1253.6 eV (1486.6 eV). UPS measurements were done with a standard He lamp, yielding 21.22 eV (He I) excitation energy. As photoelectron analyser, a VG CLAM 4 with a hemispherical energy filter and an electron detector based on discrete channeltrons was operated at 20 eV pass energy. A sputtered Au foil served as a reference for energy calibration based on the $Au4f_{7/2}$ transition at 84.0 eV.

Si-substrates were also used for the secondary ion mass-spectroscopy (SIMS) investigation so to provide better analytical response. The RF plasma effectively heats thin substrates, resulting in uncontrolled crystallisation during deposition (see Figure S1). Therefore we have used DC sputtering to secure the amorphous state of In_2O_3:H_2O film, which should be thick enough for the meaningful depth resolved SIMS. Our long-time experience revealed no principle difference in optical and electrical properties of the RF- and DC-sputtered In_2O_3:H films crystallised from a fully amorphous state. A mid-frequency pulsed (65 kHz, τ = 3.2 µs) DC magnetron sputtering was conducted in the deposition system A600V7 (Leybold Optics Dresden GmbH) at 75 mm target-to-substrate distance. The power density was 2.67 W/cm^2, total pressure—0.4 Pa, partial pressures of oxygen (O_2) and water (H_2O) during processing were 2.3 $\times$ 10^{-4} Pa and 1.7 $\times$ 10^{-4} Pa, respectively. The deposition took place on an oscillating substrate. In_2O_3 films were deposited under the same conditions but without introducing water vapour. The annealing took place in UHV at 220 °C for 30 min.

All SIMS depth profiles in this work were performed employing the CAMECA SC Ultra instrument operating under ultra-high vacuum (UHV) of ~4 $\times$ 10^{-8} Pa. A Cs^+ primary beam with an impact energy of 3 keV and intensity of 10 nA was scanned over the (150 $\times$ 150) µm^2 area, whereas the analysis was limited to the (50 $\times$ 50) µm^2 area. The positive ion detection mode was used and thus each element was measured as the CsX^+ cluster. Subsequently, a point-to-point normalisation to the Cs^+ signal was performed. Thus, due to a significant reduction of the matrix effect [15–19], we were able to detect adequately the In/O and H/O ratios as well as the annealing losses. The latter were determined as follows:

$$L_{\mathbf{H}} = 1 - \frac{I_{\mathbf{H}\ annealed}}{I_{\mathbf{H}\ as-deposited}},\ L_{\mathbf{O}} = 1 - \frac{I_{\mathbf{O}\ annealed}}{I_{\mathbf{O}\ as-deposited}} \quad (1)$$

where *I*—are the intensities normalised to the Cs signal and $L_{\mathbf{H}}$ and $L_{\mathbf{O}}$ are the relative annealing losses of hydrogen and oxygen, respectively. Despite the reduced detection limit for hydrogen in the positive ion detection mode, its concentration in water containing samples was found to be high enough for a reliable determination.

Fourier-transform infrared spectroscopy (FTIR) was performed on a Vertex 70 (Bruker Optics, Ettlingen, Germany) using the rock solid interferometer, mercury (Hg) IR-source, DLaTGS IR-Detector and the KBr Beam-splitter. In_2O_3:H films were deposited on double-side polished Si-substrates for this investigation. XRD patterns were recorded using Cu K_α radiation in different scanning modes: symmetrical Bragg-Brentano and asymmetrical detector scan. In the *in-plane* measurement, both incident and diffracted beams had grazing angles to the sample surface. D8 Discover (Bruker, Karlsruhe, Germany) and X'Pert MRD Pro (PANalytical, Almelo, The Netherlands) diffractometers were used for these tasks. LaB_6 powder (660c) was used as a standard for estimation of the crystallite size. The Hall mobility of charge carriers was measured with an Ecopia HMS-3000 system (Anyang-city, Gyeonggi-do, Korea) in van der Pauw geometry at room temperature. The proportionality factor was taken equal to 1. Scanning electron microscopy (SEM) was made using a Hitachi S4100 microscope (Hitachi High-Technologies Corporation, Tokyo, Japan).

Samples for cross sectional transmission electron microscopy (TEM) were prepared by gluing the thin films face-to-face, followed by mechanical and ion thinning for electron transparency. TEM investigations were performed on two microscopes. The Philips CM12 (FEI Company, Hillsboro, OR, USA) was used at 120 kV accelerating voltage for preliminary investigation. The system Zeiss LIBRA 200 FE (Carl Zeiss Microscopy, Jena, Germany) operated at 200 kV accelerating voltage was used for more detailed analysis by electron energy loss spectroscopy (EELS). This microscope is equipped with an in-column energy filter for energy filtered image acquisition. The set electron energy loss was varied from 0 to 30 eV.

3. Results

3.1. Crystallinity versus Electron Mobility

The crystallinity of TCO films, i.e., the size of grains and the texture, can determine electron mobility to a different extent, which depends on the individual material. According to the band structure calculations accepted for In_2O_3, conduction band minima are formed by the 5 s states [20–22]. Because of their spherical symmetry, one may then expect no significant impact of the coherence between grains (texture) onto the grain boundary scattering. However, a limiting role of the grain boundaries themselves (grain size) illustrates the following fact: the undoped single crystalline In_2O_3 films and In_2O_3 single crystals demonstrate an electron mobility of more than 100 cm^2/Vs [23,24] whereas the as-prepared polycrystalline films do not reveal μ_e exceeding 50–60 cm^2/Vs [25,26]. This fact is basically related to the difference in N_e, which is known to be much lower in single crystals (~10^{17} cm^{-3}) as compared to the polycrystalline materials (10^{19} cm^{-3}) [23]. In turn, high N_e values in polycrystalline In_2O_3 are usually attributed to the so called unintentional doping caused by the presence of water in ambient air. Additional negative impact on mobility provide ionized impurities.

In this work, we intended to examine to what extent the grain size and texture determine Hall mobilities in In_2O_3:H films. Figure 1 presents the X-ray patterns and Hall mobility data for various as-deposited and annealed films. Here, two series of experiments were done: variation of the film-thickness (*a*) and variation of the total pressure during deposition (*b*). As one may see from the series (*a*), all ≥200 nm thick In_2O_3:H_2O films appear to be X-ray crystalline. Diffraction maxima are, however, quite broad. As we explained above, this is due to the heating of the surface by the RF plasma. This effect increases with time due to the NIR absorption of the growing film and at some point the film becomes crystalline (see Figure S1).

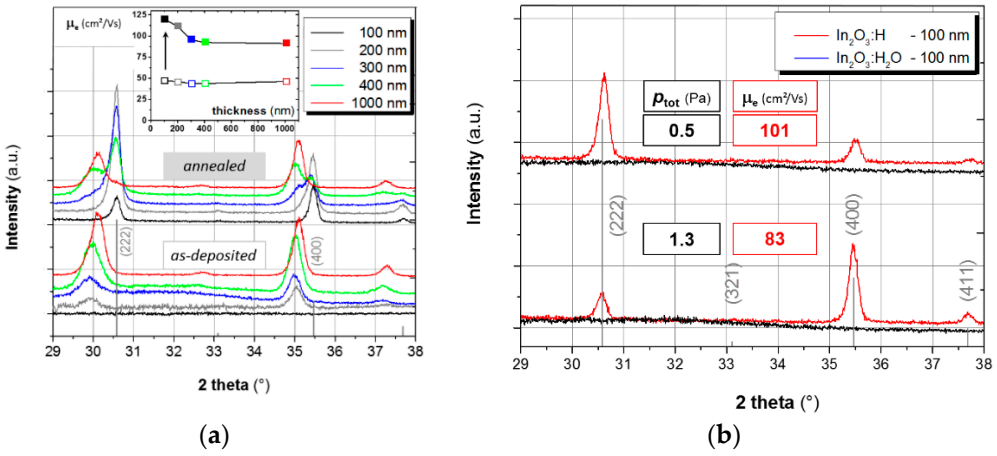

Figure 1. XRD patterns and Hall-mobility data for the RF sputtered In_2O_3:H films: (**a**) variation of thickness at p_{tot} = 0.5 Pa; (**b**) variation of the sputtering pressure at a fixed film thickness. In all cases the as-deposited state (In_2O_3:H_2O) is compared with the annealed one (In_2O_3:H). The cubic In_2O_3 powder standard (ICDD Nr. 00-006-0416) is shown in grey bars.

Post-deposition annealing at 180 °C for 60 min in ambient air results in further crystallisation and increase of electron mobility. The biggest gain of mobility is demonstrated by thinner, initially X-ray amorphous, films. All partially crystalline In_2O_3:H_2O films thicker than 300 nm reveal almost the same gain of mobility after annealing. Analysing XRD patterns in Figure 1a, one can find two In_2O_3 phases: initially crystalline and crystallised after annealing. A coexistence of two phases is especially well visible in the 400 nm thick film. Correlating this with Hall mobility data, we conclude that exactly the post-deposition crystallisation is crucial for high mobility. Interestingly, the "high-mobility" phase reveals a smaller lattice constant than the phase, which crystallises during deposition. The origin of this difference will be discussed below.

A decrease of intensity of diffraction peaks is observed for the initially crystalline In_2O_3 phase as a result of annealing. The most probable reason for that is active recrystallization.

Figure 1b demonstrates the influence of the sputtering pressure on the crystallisation behaviour of X-ray amorphous films. Apparently, this parameter determines the film texture and Hall mobility. We attribute this effect to the amount of hydroxyl in a film. Indeed, using a fixed leak rate of the needle valve feeding water vapour, a higher p_{tot} should result in a smaller $p(H_2O)$ and, hence, in a smaller concentration of hydroxyl in In_2O_3. In turn, the impact of hydroxyl on the crystalline growth of In_2O_3 is a known phenomenon, thus, the (400)-orientation can be suppressed if water is present in a sputtering gas [27]. This is consistent with our results. A higher process pressure itself may also contribute, as it increases the energy transfer from plasma to substrate, resulting in a higher deposition temperature [28].

Considering the cubic bixbyite structure of In_2O_3, one can distinguish two kinds of InO_6 octahedrons which interconnect either by corners or by edges [29]. As the octahedrons are directed along the [111] axes in the lattice, the close packed oxygen layers coincide with the {00*l*} planes. This explains why the <00*l*> oriented films might reveal a smaller electron mobility.

In our further XRD, TEM and SIMS investigations we used the ~150 nm thick films. XRD measurements (see Figure S2) were performed to estimate the size of coherent scattering in both lateral (D_{lat}) and longitudinal (D_{long}) directions using Scherrer's method [30]. In case of lateral size the asymmetric *in-plane* XRD measurements at $\psi = 89.2^\circ$ were performed. Assuming single strength and linear $d_{hkl} - \sin^2\psi$ dependence we estimated the residual stress in the films. A complex recalculation which takes into account the measurement conditions was performed on the basis of a procedure explained elsewhere [31]. The elastic constants for In_2O_3 were taken from literature [32,33]. Our results are collected in Figure S2 and Table 1. Hall measurement data are also presented for the assessment.

Table 1. Results of the XRD analysis and electron Hall-mobility data for the differently prepared ~150 nm thick In_2O_3 films on glass. The Roman numerals are used in the text for easier distinction of the film states.

States	I. In_2O_3 As-Deposited w/o Heating	II. In_2O_3:H_2O As-Deposited w/o Heating	III. In_2O_3:H_2O As-Deposited T_{dep} = 160 °C	IV. In_2O_3:H T_{ann} = 180 °C, Ambient Air	V. In_2O_3:H T_{ann} = 230 °C, UHV
D_{long} (nm)	35 ± 6	-	50 ± 15	165 ± 6	328 ± 5 *
D_{lat} (nm)	22 ± 2	-	32 ± 2	230 ± 60	205 ± 20
Residual Stress (GPa)	-2.1 ± 0.8	-	-1.9 ± 0.6	-0.5 ± 0.1	-0.6 ± 0.2
μ_e ($cm^2/V{\cdot}s$)	22	47	41	117	118
N_e (cm^{-3})	4.58×10^{20}	5.85×10^{20}	2.03×10^{20}	2.24×10^{20}	2.57×10^{20}

* This value has no real physical meaning, because the film is considerably thinner.

We see that the crystalline state itself does not secure high electron mobility: compare, for instance, the crystalline state III with the amorphous state II—both films were deposited in the presence of water vapour. The positive impact of water on μ_e is, however, obvious (compare state I with other states). This effect is explained in literature by a passivation of dangling bonds with hydrogen that decreases the electron scattering [9]. One can see that such passivation is highly pronounced exactly in the amorphous state with the utmost amount of dangling bonds (compare state II with I or III). We observe that μ_e strongly increases with the grain size, compare states III $\rightarrow$ (IV, V). Thus, both qualities: the degree of crystallinity and the passivation of dangling bonds are important for reaching a high electron mobility in In_2O_3.

It should be noted why the concentration of free electrons changes. The presence of water does not result in a marked change of N_e (compare states I and II), but high temperature does. This effect will be discussed below.

One has to notice the presence of residual compressive stress in crystalline films, especially if crystallisation takes place during deposition (states I and III). The values presented are just an

estimation with a large error, based on the measurements of only two ψ values. Two reflexions (222) and (400) with quite similar Poisson's ratio were taken into account [33].

It is a fact that in the presence of water the growing In_2O_3 films contain hydroxyl groups [9]. Moreover, the hydroxylation apparently stipulates the amorphous state of In_2O_3 [34]. We have, however, made some curious observations in our experiments, which cannot be easily explained. Thus, the In_2O_3:H_2O films (state II in the Table 1) grow predominantly X-ray crystalline on such substrates like molybdenum-films, *i*-ZnO, Si-wafer, or CIGS-absorber [11]. Moreover, if any additional oxygen is injected into the sputtering gas, the films becomew crystalline and resistive.

3.2. Presence and Role of Metallic Indium

Since the films appearing as X-ray amorphous could still be nano-crystalline, we undertook TEM investigations of them. Figure 2 shows cross-sectional brightfield TEM images of an In_2O_3:H_2O film deposited at p_{tot} = 0.5 Pa on glass.

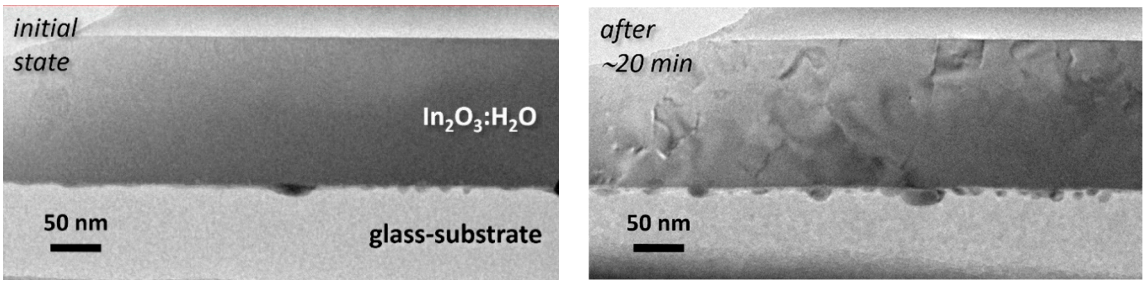

(**a**) (**b**)

Figure 2. Brightfield TEM images of the as-deposited In_2O_3:H_2O film: (**a**) first minutes of observation; (**b**) after about 20 min under the electron beam.

Several effects can be observed. Initially, the film is amorphous, but it changes under the electron-beam after about 20 min. A diffraction contrast becomes visible, indicating crystalline structures. At the same time, droplet-like features at the film/glass interface increase in number and size. Being aware of the inherent effects of our fabrication procedure, we presume here an effect of the sample heating by the e-beam. Basically, heating of TEM-lamella due to inelastic interactions with high energy electrons is a known phenomenon [35]. According to the literature, relatively thick In_2O_3:H films crystallise at 180–200 °C [1–3]. In our special case we deal with much thinner lamella, where the impact of surface and contact interface is apparently larger. This fact may shift the crystallisation temperature to lower values. Apart from the crystallisation effect observed, we assume that the appearance of droplet-like features is related to the presence of metallic indium. Its melting (T_m = 156.6 °C) might promote In_2O_3:H_2O crystallisation and results in accumulation of In-droplets.

Actually, the appearance of metallic indium seems to be rather probable in our case as the metallic phase was found in In_2O_3 and In_2O_3:Sn films by other investigators [36,37]. Consideration of the In-O phase diagram and general chemistry of indium oxide/hydroxide system also supports this assumption [34,38].

We applied energy filtered TEM to detect metallic indium, as it exhibits a bulk plasmon with an energy of about 12 eV [39]. The plasmonic spectrum of In_2O_3 [40] could not be observed in this study. The set of TEM images obtained at distinct loss energies is presented in the Supplementary Materials (Figure S3). Metallic indium appears as bright areas at an electron energy loss of ~12 eV. We also found that indium congregates either at the film-glass interface or localises in the bulk (see Figure S4). The latter case is shown in more detail in Figure 3, where the correlation of crystallinity (Figure 3a) and appearance of metallic indium (Figure 3b) can be observed. The top In_2O_3 layer grows crystalline due to the impact of RF plasma as we discussed above. The crystalline part consists of columnar crystallites of 20–40 nm lateral size, which is consistent with the film state III in Table 1. One can conceivably detect

some porosity within this area (see Figures 3a and S3). Metallic indium particles segregate exactly at the transition region between amorphous and crystalline layers (Figure 3b). These nanoparticles were found to be crystalline (Figure S5). Obviously, melting of indium and hence its extraction in a separate phase is associated with indium oxide crystallisation. The liquid phase is known to support even high quality crystallisation in such methods as liquid phase epitaxy [41], metal-modulated epitaxy [42], volatile surfactant assisted chemical vapour deposition [43] and others.

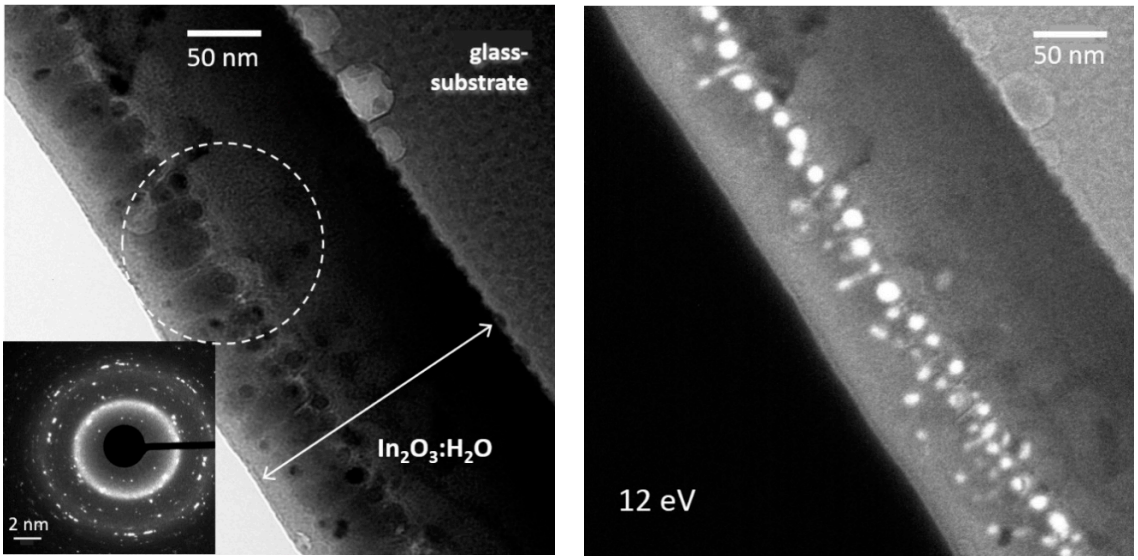

(**a**) (**b**)

Figure 3. Medium magnification bright field image (**a**) and EFTEM image at an electron energy loss of 12 eV (**b**) obtained on an as-deposited In_2O_3:H_2O film at the same location. Image (**a**) elucidates two parts of the film: the bottom ~100 nm thick amorphous part and the top ~50 nm thick crystalline part. The electron diffraction pattern is obtained for the region, marked by a circle. Bright regions in the figure (**b**) correspond to metallic indium.

3.3. Optical Properties of In_2O_3:H_2O and In_2O_3:H

Optical measurements allow determining properties of the continuous matter. If a material is crystalline, we receive the information from the interior area of grains, whereas the electrical properties are cumulative. Many optical investigations of In_2O_3 and In_2O_3:H films have been undertaken [2,36,44,45]. According to S. Joseph and S. Berger, the fitting of IR optical transmission spectra by effective medium approximation reveals that no changes in In_2O_3 transmittance should be observed if the volume fraction of metallic indium remains less than 10%. A larger indium excess results in a markedly lower transmittance as compared to that experimentally observed [36]. The presence of a metallic phase can be also deduced from the temperature dependence of the resistivity [46]. This, however, demands an even higher volumetric content of indium for the percolation of electrical current.

Figure 4 presents fitted optical spectra for the thin films. The fits were obtained with the help of the RIG-VM software developed at Fraunhofer IST [47]. A Tauc-Lorentz oscillator has been used for the fundamental absorption and a Drude term for the free electrons. A free electron mass of $m^* = 0.28\ m_e$ has been used [23]. As one can see, the optical mobility matches well with the Hall mobility (compare with Table 1) for both film states. Some deviation is observed for the crystalline state, where the Drude term gives a somewhat smaller mobility. This can be attributed to the insufficient spectral range to fit the plasma resonance of free carriers accurately. A remarkable difference in N_e values should be noted, namely, the electrical measurements gave an approximately double concentration of free electrons, which are not visible optically. This means that we might observe an additional inter-grain source of free electrons.

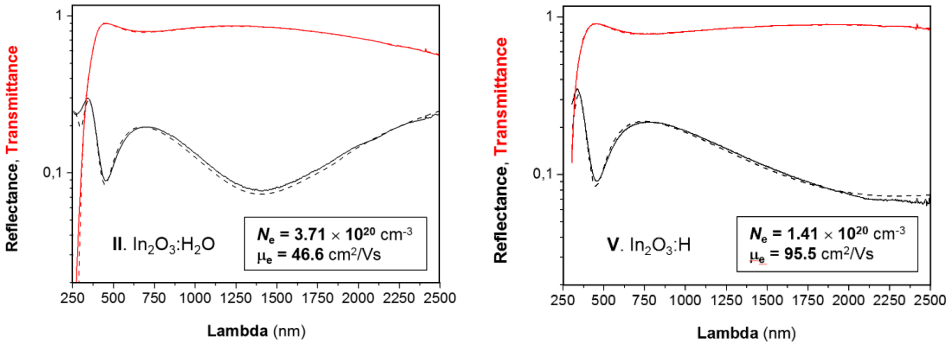

Figure 4. Fits (dashed lines) of the optical spectra (solid lines) for ~100 nm thick In_2O_3:H_2O (**a**) and In_2O_3:H (**b**) films on glass. The μ_e and N_e values identified from the fitted spectra are given. Corresponding plasma edges, film thicknesses and mean square errors are as follows: (**a**) λ_p = 916.918 nm, d = 103.385 nm, MSE = 0.00757124; (**b**) λ_p = 1486.62 nm, d = 104.554 nm, MSE = 0.00893229.

Based on the measurements in the UV range, we determined optical band gaps based on the Tauc-Lorentz model. These values are presented in Table 2 for the material states I, II and V.

Table 2. Results obtained from the optical absorption of variously prepared In_2O_3 films.

States → Band Gap/Thickness ↓	I. In_2O_3 As-Deposited w/o Heating	II. In_2O_3:H_2O As-Deposited w/o Heating	V. In_2O_3:H T_{ann} = 230 °C, UHV
E_g (eV)/100 nm	3.55	3.46	3.68
400 nm	3.50	3.48	3.65

According to the literature, there cannot be an indirect gap in pure In_2O_3 due to the parabolic nature of the conduction band [22]. Moreover, the minimum band gap at 2.9 eV is symmetrically forbidden and the first allowed optical transition occurs from the level ~0.8 eV below the valence band top that gives the commonly observed value of $E_g \approx 3.7$ eV. As presented in Table 2, the as-deposited crystalline In_2O_3 films (state I) reveal considerably lower E_g as compared to the expected value for this material. Amorphous films, which probably contain water (state II), demonstrate even lower values; however, for 400 nm thick films the difference between states I and II is negligible. This is consistent with the fact of partial crystallisation observed in thicker In_2O_3:H_2O films (see Figures 1 and 3). However, no influence of water in the state II is then noticed. We do not detect the influence of expected hydrogen doping in the post-crystallised In_2O_3:H films (state V) as well, because the optical E_g values observed are very close to the ones known for the pure In_2O_3.

3.4. Chemical Changes in In_2O_3

To understand if there is any chemical transformation during crystallisation and which doping mechanism is realised, we performed further investigations. According to the FTIR analysis (data are not presented in this paper) none of the OH or adsorbed water (1615–1630 cm^{-1}) features were observed in crystalline films. This might mean that these species, if they exist, are concentrated mainly at the grain boundaries. The IR transmittance, however, differs considerably for different film states. Thus, an addition of water during deposition results in a significant reduction of the IR transmittance (states I and II are compared). Annealing in vacuum does not significantly change it (states II → V), whereas annealing in ambient air provides quite a strong increase of the IR transmittance (states II → IV). Taking into account our TEM/EELS results, we attribute this behaviour to the presence of metallic indium in the films deposited in the presence of water. Annealing of such films in ambient air provides more effective oxidation of indium as compared to the annealing in vacuum.

SIMS was used to determine the In/O and H/O ratios across the film. As we pointed out in experimental section the DC-sputtered~150 nm thick In_2O_3 films were analysed in this case. Figure 5a compares the In/O ratio in as-prepared and annealed films deposited with and without water. As one can see, In_2O_3 films contain less oxygen and do not change during annealing in vacuum. According to our visual observations, In_2O_3 films are usually darker than In_2O_3:H films. Therefore, we assume the In_2O_3 to be oxygen deficient. On the contrary, very transparent In_2O_3:H films seem to possess a stoichiometry close to $x = 3$ in In_2O_x. Curiously, we observe the same oxygen enrichment profile in the upper ~50 nm of both: as-deposited and annealed In_2O_3 films. At the very surface this enrichment approaches the overall level observed in the annealed In_2O_3:H film. As this effect is insensitive to annealing, we most probably deal with the impact of a short exposure to the ambient air prior to the measurement. It is observed only in the case of tiny crystalline, sub-stoichiometric films, which indicates a reaction in the inter grain space.

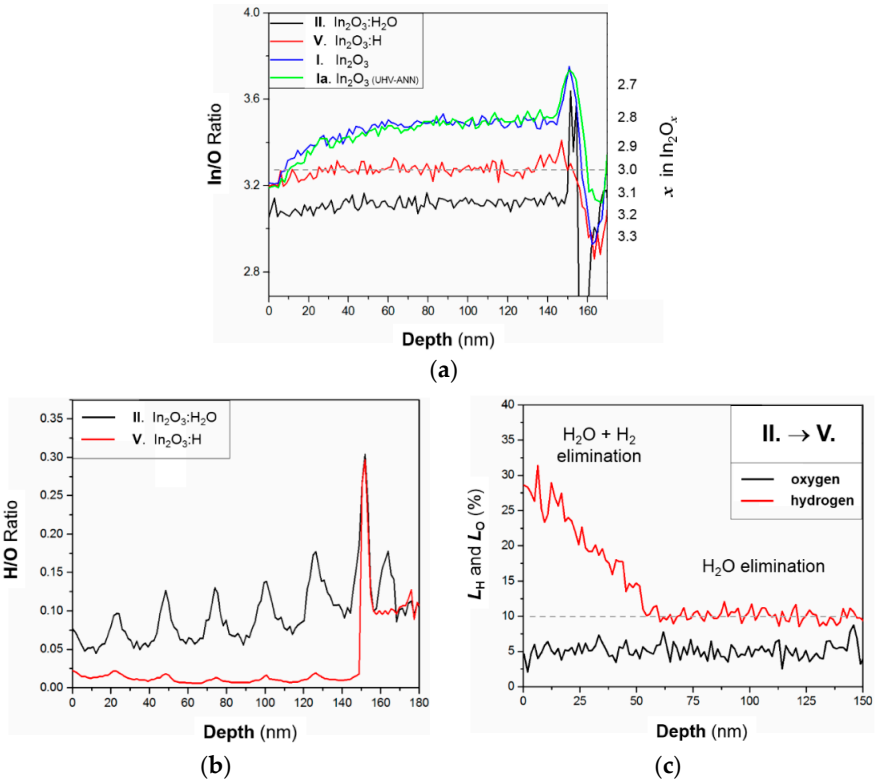

Figure 5. SIMS depth profiles obtained on various ~150 nm thick DC sputtered In_2O_3 films. Indium to oxygen concentration ratios (**a**) were obtained for the film states I, II and V, which correspond to the Table 1. State Ia represents the UHV-annealed In_2O_3 film. Hydrogen to oxygen concentration ratio (**b**) and the percentage losses of hydrogen and oxygen (**c**) are compared for the as-deposited and annealed states of the film, intentionally containing water.

Water containing, as-deposited films (state II) have the highest oxygen content among the investigated systems. It decreases after annealing (state V) together with the increase of transparency in both UV and near IR spectral regions. We attribute this oxygen loss to the release of water, as the In/O ratio remains unchanged in the water-free In_2O_3 sample under the same treatment. Furthermore, active oxygen diffusion in In_2O_3 starts at temperatures above 600 °C [48].

For better understanding, we represented the measured data in the form of an H/O ratio (Figure 5b) and the percentage loss of hydrogen and oxygen (see formulas (1)) as a result of the annealing (Figure 5c). Obviously, hydrogen-to-oxygen ratio is higher in as-deposited state. Its depth profile demonstrates several pronounced maxima, which correspond to the substrate oscillation and passing by the inlet of water vapour. This result validates our procedure of hydrogen detection,

proving the satisfactory sensitivity, which we can only achieve for the water-containing films. On the other hand we realise that hydrogen detected in as-deposited films represents most likely just water. A comparison of L_H and L_O discloses an interesting effect: the oxygen loss remains stable over the entire film thickness, whereas hydrogen releases more actively from the top but demonstrates a stable L_H in the depth. We suggest the release of H_2O and H_2 species from the film being annealed (Figure 5c), as only their formation in a free volatile form is chemically possible. Water can evaporate in its free form if it is contained or released from the hydroxyl groups as shown in the reaction (4) below. Hydrogen would form only in the presence of metallic indium according to the reactions:

$$In + 3\ H_2O \rightarrow In(OH)_3 + 3/2\ H_2 \quad (2)$$

$$In + In(OH)_3 \rightarrow In_2O_3 + 3/2\ H_2 \quad (3)$$

The probability of such reactions and some supporting experimental data published will be considered in the discussion chapter below.

Considering SIMS results, we could not operate with the absolute values since we did not use any external standard. However, the qualitative suggestions made were based on internal standards—indium and oxygen. We realised that the crystallised In_2O_3:H film, which is a high mobility TCO to be used in various devices, might suffer from the chemical heterogeneity.

To observe the processes taking place on the film surface, UPS and XPS measurements were undertaken. Our XPS measurements (spectra are not shown here) reproduced the results obtained by Hans F. Wardenga, where In_2O_3:H_2O films revealed a shoulder at the O1s emission line at about 532.6 eV binding energy [9]. This was found to correspond to the OH bonds, which disappear after annealing.

The UPS spectra acquired during a stepwise increase of temperature from the ambient level (~25 °C) up to 230 °C in UHV show the following changes in the In_2O_3:H_2O film (Figure 6). A ~0.4 eV shift in the secondary electron edge is observed. The secondary electron edge can be used to determine the work function of a material according to the relation $W_f = E_{ex} - EB_{sec}$. Thus, we observe here the W_f change from ~4.0 eV to ~4.4 eV that basically contradicts the doping phenomenon. It is worth noticing that the work function of the thermally deposited fully oxidised indium oxide is 5.0 eV [49]. This means that indium in the films in question has a lower oxidation state than in the stoichiometric oxide. The value of W_f is also determined to a large extent by the crystallographic orientation [50]. In our case the observed increase of a work function is probably caused by the appearance of a distant order. The significant difference relative to the fully oxidised In_2O_3 state can be connected to the presence of metallic indium in the films (our TEM and FTIR data).

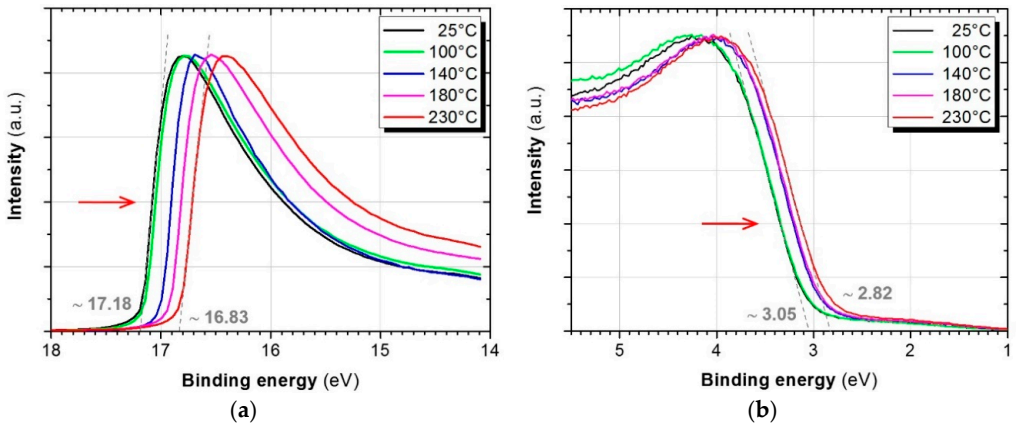

Figure 6. UPS spectra obtained for the ~150 nm thick In_2O_3:H_2O films during stepwise annealing in UHV without breaking vacuum. Two regions (**a**,**b**) of the same spectra are shown. For comparison, the intensity was normalised and the background was removed. The excitation energy was 21.2 eV.

According to the Figure 6b, vacuum annealing causes a shift of the valence band edge by ~0.2 eV. All observed changes are be depicted on the energy diagram, where the UPS data are used to fix the E_F and E_{VB} levels (Figure 7). Here we used a caption $E_{g,\,min}$ (minimum) for the fundamental band gap, which is known to be 2.9 eV for the pure In_2O_3 [23]. If we admit any doping in our films, it can be even smaller due to the band gap narrowing phenomenon [51,52]. The optical $E_{g,\,opt}$ values obtained in this study were placed in accordance with the principle described above [22]. These energy diagrams show that the Fermi level is very close to the conduction band in both materials: amorphous and crystalline. If we admit the same fundamental band gap width for both states, then the latter would be a non-degenerate semiconductor that should not be the case for such high concentration of free electrons. Since we observed a Burstein-Moss shift as a result of the annealing, the In_2O_3:H likely remains degenerate due to the band gap shrinkage. Major changes happen with a level of the allowed optical transition inside the valence band, namely, it shifts markedly downwards. This can be attributed to the effect of crystallisation as the valence band contains fully occupied 2*p* and 2*s* oxygen states and empty 4*d*-indium states [22].

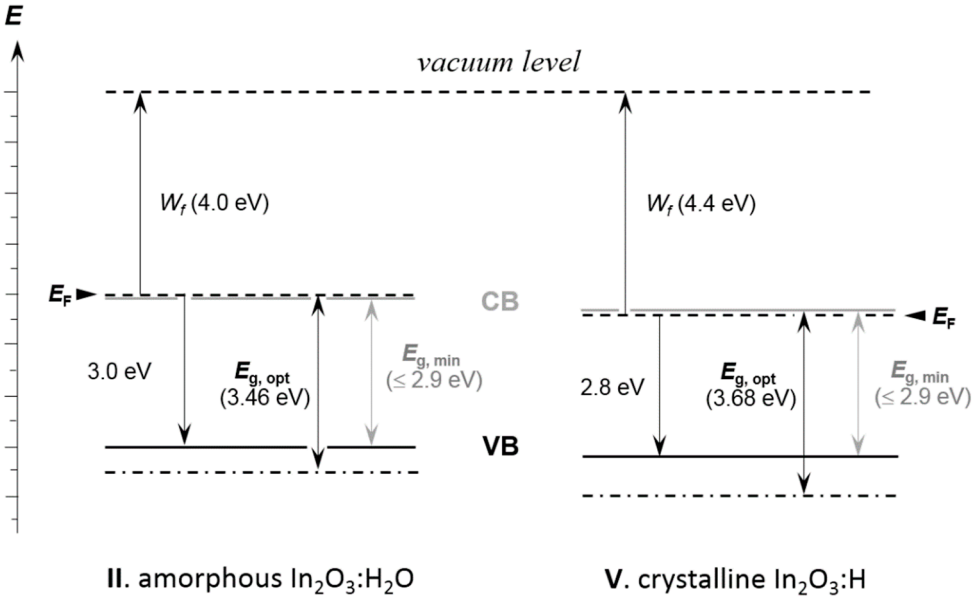

Figure 7. Energy diagram for indium oxide of the states II and V. The scheme is created on the basis of optical (UV-Vis) and UPS data.

The observations made require a more detailed discussion of the In_2O_3 chemistry and possible origin of doping.

4. Discussion

To understand the results obtained in this work, we have to review some basic properties of indium, In_2O_3 and $In(OH)_3$.

4.1. Appearance of Metallic Indium in In_2O_3

The electro-chemical potential of metallic indium is $\varphi^0 = -0.3382$ V [53]. This means that under normal conditions, metallic indium should not reduce protons in an aqueous solution to molecular hydrogen. Nevertheless, the potential is not too high and both reactions, reduction of metal and reduction of hydrogen, may proceed simultaneously on a competitive basis.

According to the In-O phase diagram, there is no detectable phase of oxygen non-stoichiometry [38]. If any In-excess is provided ($\geq$0.02 at.%), there is a mixture of two phases: In_2O_3 and metallic In, which is solid below 156.634 °C and liquid above this temperature. Indium

(III) oxide is thermodynamically very stable over a wide range of T and $p(O_2)$. According to the Ellingham diagram, one needs a $p(O_2)$ of about 10^{-100} atm. in order to reduce it to metallic indium at room temperature. The equilibrium oxygen partial pressure at 200 °C is about 10^{-55} atm. At the same time, metallic indium remains stable in air and starts to oxidise visibly only after melting. The oxidation of indium in a liquid form proceeds about five time faster as compared to the solid [54]. Aside from the main oxidation state +3, indium may have also +2 and +1 in combination with oxygen. A formal oxidation state +2 is most probably a mixture of diamagnetic +1 ($5s^2$) and +3 ($5s^0$) forms, as no experimental evidence of magnetism in reduced indium oxides was detected. The theoretical investigation of hypothetical neutral, molecular In-O clusters with different In/O ratios reveals their high instability in an ionic environment [55]. The HOMO–LUMO gap was found to depend on the metal-to-oxygen ratio in the cluster. Oxidation is likely unfavourable when the In/O ratio is larger than 1, as both vertical and adiabatic electron affinities are negative for In_2O. In oxygen-deficient In_2O_3 films, metallic indium may form as a result of oversaturation by cooling down after deposition at elevated temperature [36]. In this case, indium precipitates according to HRTEM and EELS in a form of 5–30 nm nano-particles independently of an indium excess. It is known that intermediate oxides disproportionate in contact with water, resulting in In_2O_3 and metallic indium [34]. These data confirm that metallic indium readily forms if any lack of oxygen and/or water is provided.

To understand the chemical impact of water during sputtering, let us briefly consider the plasma chemistry of water. Basically, low total pressure and especially plasma excitation change the chemical activity of water. Upon photo-ionisation, water vapour becomes a weakly ionised plasma consisting of electrons and H_2O^+ [56]. In the highest state of excitation, the plasma consists of e^-, H^+, and $O(^{n+})$. In a general case of RF-sputtering from the ceramic target, mostly M^+ and MO^+ charged species are observed [57]. In the case of In_2O_3, the RF plasma should contain these species in a ratio M^+/MO^+ of more than 30. Since this ratio depends on the M-O binding energy, we took the value known for Fe_2O_3 implying that the M-O binding energy is quite close for Fe_2O_3 ($\Delta G^\circ_{298} = -732.1$ kJ/mol) and In_2O_3 ($\Delta G^\circ_{298} = -809.3$ kJ/mol) [58,59]. When argon is used as a sputtering gas, almost no O^+, but mostly neutral oxygen is observed [58,60]. The RF-plasma above the ZnO target has a similar content; however, oxygen species generated during DC sputtering of ZnO are O^-, $O_2{}^-$, and O. The content of negatively charged oxygen species increases exponentially with the reduction of the total pressure [61]. The main difference between the RF and the DC process lies in the concentration of electrons, which is much higher in the first case. Thus, in our process, we likely deal with an intermediate oxidation state of indium in the absence of strong oxidants in the plasma, which finally yields metallic indium species in a film.

4.2. Water Containing In_2O_3

Despite a chemical impact as hydroxylation, water stipulates the amorphous state of as-deposited films. It is known that indium (III) hydroxide tends to remain jelly or even forms a colloid in aqueous solutions rather than precipitating in a crystalline form. The main reasons for that are the donor-acceptor interaction, typical for metals having free 3*d* orbitals, and the hydrogen bonding in hydroxides. As it is known for the most investigated analogue—aluminium hydroxide, such parameters as concentration, temperature and pH determine the hydrolysis, peptisation, aging and, finally, crystallisation [62]. Basically, al least three processes are coupled with water release and formation of many networking chemical bonds:

$$\text{=In-OH + HO-In=} \rightarrow \text{=In-O-In= + } H_2O \quad (4)$$

According to the thermal gravimetric analysis, the crystalline $In(OH)_3$ transforms into In_2O_3 with water elimination, starting very slowly from T $\geq$ 200 °C and becomes fast at about 230 °C in an inert 1 bar atmosphere [63]. As per Le Chatelier's principle, the dissociation in vacuum likely proceeds at lower temperature.

It is known that gaseous hydrogen can also be successfully applied as a hydrogenation agent yielding high-mobility In_2O_3 films [64]. In this case, the films were obtained by RF sputtering in an amorphous state as well and crystallised by post-deposition annealing. Thorough investigation of oxygen and hydrogen desorption from the In_2O_3 powders with different surface areas serves us with the following observations [10]. Surface hydrogen starts to desorb in a high vacuum ($p = 5 \times 10^{-7}$ mbar) already at temperatures somewhat below 100 °C. Desorption of stronger bound hydrogen starts at ~150 °C. Water (6 mbar in 1 bar He) becomes an active re-oxidation agent at temperatures higher than about 250 °C, whereas dry oxygen (1 bar) actively re-oxidises the surface starting from >150 °C.

Thus we realise that hydroxylation of In_2O_3 is most likely the reason for the amorphous state of as-deposited films. This effect can be achieved via sputtering in the presence of either hydrogen or water. Hydrogen acts even more reproducibly [64], since it probably delivers just a necessary hydroxylation without any water excess. However, we still need to understand the desorption of chemically different hydrogen. Additionally, the effect of In_2O_3 reduction in hydrogen on its electrical conductivity should be considered.

4.3. Doping and Conductivity of In_2O_3

It is known that oxygen deficiency in In_2O_3 causes higher conductivity [10,46,65]. According to the impedance measurements performed on In_2O_3 polycrystalline samples, their reduction in dry hydrogen results in a slow resistance decline, starting already at room temperature. The resistance falls sharply at a temperature somewhat below 100 °C and further decreases much slower up to its minimum at about 250 °C [10]. In the presence of water, the same dependency is observed, but the temperatures are about 50 °C higher. This change is reversible and matches the hydrogen adsorption/desorption data; however, the resistance of the re-oxidised samples was found to be 4–5 orders of magnitude lower than the initial one. It might point to the inter-grain changes, e.g., In_2O_3 reduction, which is then encapsulated by the fully oxidised shell.

We already showed above that the concentration of electrons and hence electron mobility in In_2O_3 films were often found to be determined by the size of crystallites [23]. In the literature this effect is attributed to the so-called unintentional doping, which is supposedly caused by the inter-grain diffusion of water from ambient air [66,67]. The mechanism of such doping, however, remains questionable for us.

Theoretical studies of this matter demonstrate quite discrepant conclusions. Some basic description of the defect chemistry in In_2O_3 was done, using solid state chemistry [68]. However, most modern investigations being aimed to justify which point defects exist in the material are performed using density functional theory (DFT). Thus, according to J. Liu, who used the GGA + U formalism, the most stable point defects in In_2O_3 crystals are oxygen vacancies of the anti-Frenkel type ($V_O^{\bullet\bullet}$-O_i'') [69]. According to the LDA and LDA+U functional calculations, the formation energy of V_{In}''' was found to be very low in *n*-type In_2O_3 [70]. Considering hydrogen doped In_2O_3, S. Limpijumnong with co-workers suggested $H_i^{\bullet}$ and $H_O^{\bullet}$ as the main donor defects in In_2O_3:H rather than $V_O^{\bullet\bullet}$ [71]. A combination of theory with the muon rotation/relaxation spectroscopy revealed that the charge neutrality level (CNL) for hydrogen in In_2O_3 lies above the conductive band minimum (CBM), thus providing a shallow donor level with an activation energy of 47 ± 6 meV [66]. This study also stated that hydrogen often becomes an unintentional donor in many polycrystalline oxides. According to T. Tomita et al., who used first-principles molecular orbital calculations, the interstitial indium ions ($In_i^{\bullet}$) are the native donors in In_2O_3 [72]. These defects may only coexist with V_O (no charge was noticed in the original work), which facilitate the emergence of indium donors as shallow states.

Considering the penetration of hydrogen into indium oxide, we have to take into account the classical approach of experimentally obtained ionic radii. Oxygen ions (O^{2-}) with tetrahedral coordination, like in the In_2O_3 bixbyte structure, have an effective ionic radius of 1.38 Å [73]. The OH^-

group would have an even smaller (1.35 Å) ionic radius in this coordination, since the proton is actually a pristine positive nucleus, which is drawn in to the negative electron shell of oxygen, thus making the Coulomb repulsion between neighbouring oxygen ions smaller. On the basis of this simple consideration it is hard to imagine that the hydrogen proton or even the neutral H atom, having a Bohr radius $a_0 \approx 0.53$ Å, can replace oxygen in its site. Thus we recognise that the hydroxyl $(OH^-)_O^\bullet$ is the most probable hydrogen containing species in In_2O_3. It is known, however, that In^{+3} also shows the atomic absorption of hydrogen [74]. Hydrogen was also found to be readily adsorbed by an indium rich InP surface [75]. A large thermodynamic driving force for the neutral covalent binding between hydrogen and solid state indium dimers was identified.

The existence of interstitial indium ions has also some restrictions. Thus, In^{+3} in octahedral coordination possesses, an ionic radius of 0.8 Å is rather large to squeeze into the cavities of the bixbyite lattice. A lower indium oxidation state, e.g., +1 ($In_i^\bullet$), corresponds to an even larger ionic radius. The intermediate oxidation states are furthermore electrochemically unstable (see above). However, ferromagnetism was observed in oxygen deficient InO_x films annealed in UHV at 600 °C [65]. This effect was found to be accompanied by the In-In clustering and formation of highly defective glassy regions in crystalline In_2O_3 [65]. According to Preissler and Bierwagen, the existence of doubly ionized donors best describes the ionized impurity scattering in unintentionally doped In_2O_3 [23]. Attributing this circumstance to the existence of an indium excess, it is not unlikely to suggest such a defect as $In_O^{\bullet\bullet}$, which is the non-oxidised indium at the oxygen site. It means that we might basically have $In_{In}^\times - In_O^{\bullet\bullet} - In_{In}^\times$ clusters with an effective In^{+2} oxidation state.

As for oxygen vacancies, the main disagreement in literature concerns their energy level, which represents either deep [76] or shallow states [23,67]. A practical way to discover which point defects provide conductivity in oxide materials is to measure the conductivity or better the N_e dependence on $p(O_2)$. The main restriction on that is the requirement of an equilibrium, which for metal oxides means quite high temperatures, far beyond the typical 200–250 °C for In_2O_3:H. So the measurements performed at 800 °C discovered the $\sigma \propto p(O_2)^{1/10}$ dependence for In_2O_3. Authors attributed this dependence to the $(In_i^{\bullet\bullet\bullet}\text{-}O_i'')^\bullet$ cluster formation [77]. In other work Hall measurements are presented for In_2O_3 films obtained at different $p(O_2)$ by RF sputtering without intentional heating [78]. Conductivity was found to be rather constant (~3×10^3 $\Omega^{-1}cm^{-1}$) at low oxygen partial pressure (<8×10^{-4} Pa). When $p(O_2)$ increases, conductivity sharply drops over some orders of magnitude that is mostly caused by a decrease of N_e from ~10^{-19} to 10^{-16} cm^{-3} (at $p(O_2) \approx 10^{-3}$ Pa). The authors suggested oxygen vacancies as the major donor defects. In this case the N_e should have revealed the slope $\propto p(O_2)^{-1/6}$ for the very deficient oxide and $\propto p(O_2)^{-1/4}$ for the almost stoichiometric one. From the data presented in this paper one can derive a $N_e \propto p(O_2)^{-9}$ correlation, which cannot be explained by the defect chemistry. This can be rather easier attributed to the presence of a metallic indium phase. There is another important point supporting this hypothesis. The work function, measured for metallic indium, varies in the range from ~3.9 to ~4 eV, depending on temperature [79]. This value is very close to the one measured for In_2O_3:H_2O and slightly smaller as compared to the one measured for In_2O_3:H films (see Figure 7). This means that free electrons can easily be injected from the In^0 outer shell into the conduction band of both oxides.

We would like to point also at the very interesting effect of photo-induced change in reactively DC-sputtered amorphous In_2O_3 films: an exposure of ≤100 nm thick films to UV light ($h\nu \geq 3.0$ eV) resulted in a stable increase of conductivity by $\times 10^8$ reaching $\sigma \geq 10^3$ $\Omega^{-1}cm^{-1}$ [80]. Simultaneously, the absorption coefficient increases by up to a factor of 10^3 for $h\nu < 1.5$ eV and the absorption edge shifts by +0.1 eV. A Drude approximation of the optical absorption in the near IR region gives $N_e = 1.5 \times 10^{20}$ cm^{-3} that agrees with the Hall data. These data actually represent the pure effect of In_2O_3 reduction without hydrogenation/hydroxylation impact. They reproduce to some extent our results; however, the Burstein-Moss shift observed in presence of hydrogen is about 0.1 larger.

4.4. High-Mobility of In_2O_3:H

After T. Koida, the high mobility In_2O_3 is widely accepted to be doped by hydrogen. He also stated that the doubly ionised impurities were exchanged by singly ionised ones during the annealing process that results in about twofold reduction of N_e [44]. The in-situ Hall measurements performed by H. F. Wardenga et al. during annealing of as-deposited In_2O_3:H films in vacuum have allowed underlining the following stages [9]. The first stage elapsing at about 160 °C is accompanied with a slight decrease of μ_e, which occurs, as supposed, due to the phonon scattering being expected for the degenerated semiconductors. Within this stage N_e remains settled. During further heating from 160 °C up to 200 °C, the N_e increases and μ_e remains unchanged. At T > 250 °C, N_e starts declining fast and a strong increase of μ_e takes place. The authors suggest that the driving force of the rising N_e is crystallisation followed by the grain growth. In turn, the depletion (decrease of N_e) at grain boundaries is to be the reason of a measurable depletion in a material with small grains. Crystallisation and grain growth are superimposed by the decomposition of $In(OH)_3$. According to the authors, the release of oxygen is responsible for the drop in carrier concentration and the grain boundaries are being saturated by hydrogen, closing dangling bonds.

We may not fully agree with this explanation mainly because of the known fact that hydrogen disappears first from the inter-grain space. We believe therefore that the dangling bonds existing at grain boundaries are most probably eliminated by the reaction (4). Moreover, it is known that the undoped single crystalline In_2O_3 reveals electron mobility exceeding 200 cm^2/Vs that is restricted by ~270 cm^2/Vs due to the phonon scattering [23]. On the other hand the unintentionally doped polycrystalline samples can demonstrate similarly high μ_e as the hydrogen doped ones [44,81]. According to T. Koida the effective mass in In_2O_3:H seems to depend on N_e mostly, rather than on crystallinity [44]. Many of the experimental data collected for various In_2O_3 based systems reveal a plateau on $\mu_e = f(N_e)$ dependency exactly around $N_e \sim 10^{20}$ cm^{-3} [23]. This phenomenon is also associated with a large spread of mobilities indicating additional scattering due to imperfections in the crystal for the samples with $\mu_e < 130$ cm^2/Vs.

5. Conclusions

To conclude, we observed that the free charge carriers in both In_2O_3 and In_2O_3:H films can appear due to the presence of In^0. We suggest that metallic indium is present in as-deposited In_2O_3 or In_2O_3:H_2O films in a much, up to the atomic level, dispersed state. The presence of water or hydrogen during In_2O_3 deposition at low temperature secures the amorphous state of the film. Hydroxylation of In_2O_3 is probably the main reason for that. Crystallisation of such films starts at ~160 °C when the excess of indium agglomerates, releasing in a separate nano-crystalline phase due to the melting. Melted indium species may vanish during annealing in two ways: either via evaporation and oxidation by water in UHV or via oxidation by oxygen in air. Thus, the concentration of free electrons in In_2O_3 matrix is reduced and the near IR transparency increases. Both processes, however, do not provide high mobility. The laterally extended growth of crystallites happens when water is released as a result of the hydroxide → oxide transformation. Growing crystallites interconnect at grain boundaries by the In-O-In bonds. These factors both provide high electron mobility exceeding 100cm^2/Vs. According to our experimental observation, annealing in air demands lower temperature (~180 °C) to provide high mobility as compared to the annealing in UHV (>220 °C). We attribute this to the higher water content in the former case. Crystallisation of the In_2O_3:H_2O system is accompanied with the doping of In_2O_3. We expect that the "unintentional" doping differs from the "hydrogen" doping as follows. In the first case a spontaneous injection of free charge carriers from the dispersed In^0 metallic species concentrated in the inter-grain defect-rich spaces takes place. In the second case, we likely deal with oxidation of the intra-grain In^0 defects trapped during crystallisation by Schottky vacancies:

$$In_O^{\bullet\bullet} + 1/2\ O_2 + V_{In}''' \rightarrow In_{In}^{\times} + O_O^{\times} + e' \quad (5)$$

$$In_O^{\bullet\bullet} + H_2O + V_{In}''' \rightarrow In_{In}^{\times} + OH_O^{\bullet} + 1/2\, H_2 + 2e' \quad (6)$$

Reactions (5) and (6) describe oxidation by oxygen and water, respectively. High temperature makes water an oxidizing agent, whereas low pressure facilitates hydrogen removal. According to our SIMS results, gaseous hydrogen is removed from the film mostly from the top ~50 nm layer. Metallic indium can also accumulate hydrogen in the bulk of the film. As we saw, $OH_O^{\bullet}$ defects most probably also exist in In_2O_3:H films but their formation in the absence of In^0 is not associated with any redox reaction, so in that case they do not donate electrons.

Supplementary Materials: The following are available online at http://www.mdpi.com/1996-1944/12/2/266/s1, Figure S1: SEM cross-section of the RF sputtered (p_{tot} = 0.5 Pa) 500 nm In_2O_3:H_2O film obtained on Si-substrate, Figure S2: XRD patterns for ~150 nm In_2O_3 films deposited (RF-sputtering, p_{tot} = 0.5 Pa) on glass: comparison of crystallisation conditions. Roman numerals correspond to the film states discussed in the text. Diffraction patterns were acquired using detector-scanning at grazing incidence in the *out-of-plane* (a) and *in-plane* (b) modes, Figure S3: TEM images obtained using energy filter. The set energy is marked on each image, Figure S4: Cross-sectional TEM images acquired with electrons having 12 eV energy loss on the sample. The bright areas correspond therefore to metallic indium in as-deposited In_2O_3:H_2O film. Two types of indium segregation: on the film/glass interface (a) and within the bulk of the film (b) are observed, Figure S5: TEM image of metallic indium nanoparticles released in In_2O_3:H_2O matrix. The lattice fringe contrast observed reveals their crystalline state.

Author Contributions: R.M. planned and organised some (SIMS, TEM/EELS) measurements, developed XRD, UPS, TEM and optical data, developed ideas and written the paper. A.S. initiated the work, deposited rf-films and performed the XPS, UPS and XRD measurements. M.W. performed the TEM/EELS investigation and provided support with the corresponding text. P.P.M. performed the SIMS measurements and provided support with the text. U.B. prepared the samples for the TEM investigation and performed preliminary TEM analysis. A.P. developed the optical model for optical data. D.E. deposited the dc-films. S.K. took part in many discussions and provided support with his experience. R.K., I.L. and B.S. are the leaders of the groups involved; they provided support with their expertise as well.

Funding: This work was funded by the German Federal Ministry for Economic Affairs and Energy under contract number 0325762 (TCO4CIGS). We acknowledge support by the German Research Foundation and the Open Access Publication Funds of TU Berlin.

Acknowledgments: The authors express special thanks to their colleagues from the Bruker AXS application lab in Karlsruhe, namely, to Fernando Rinaldi and to Wolfram Pitschke for the measurements on high-end XRD equipment. We thank Christoph Genzel (Department for Microstructure and Residual Stress Analysis, BESSY II, HZB) for professional support in XRD data processing. Carola Klimm (Institute for Silicon Photovoltaics, HZB) is gratefully acknowledged for the SEM investigation which was very helpful for this work in general but went beyond this manuscript. We acknowledge Johanna Reck (Optotransmitter-Umweltschutz-Technologie e.V.) for FTIR measurements and thorough discussion of the optical data. The authors also thank Daniel Abou-Ras (Department for Nanoscaled Structures and Microscope Analysis, HZB) for fruitful discussions and for making helpful remarks.

Conflicts of Interest: There are no conflict of interests to declare.

References

1. Koida, T.; Fujiwara, H.; Kondo, M. Hydrogen-doped In_2O_3 as High-mobility Transparent Conductive Oxide. *Jpn. J. Appl. Phys.* **2007**, *46*, L685–L687. [CrossRef]
2. Koida, T.; Fujiwara, H.; Kondo, M. Structural and electrical properties of hydrogen-doped In_2O_3 films fabricated by solid-phase crystallization. *J. Non-Cryst. Solids* **2008**, *354*, 2805–2808. [CrossRef]
3. Scherg-Kurmes, H.; Koerner, S.; Ring, S.; Klaus, M.; Korte, L.; Ruske, F.; Schlatmann, R.; Rech, B.; Szyszka, B. High mobility In_2O_3:H as contact layer for a-Si:H/c-Si heterojunction and mc-Si:H thin film solar cells. *Thin Solid Films* **2015**, *594*, 316–322. [CrossRef]
4. Koida, T.; Fujiwara, H.; Kondo, M. High-mobility hydrogen-doped transparent conductive oxide for a-Si:H/c-Si heterojunction solar cells. *Sol. Energy Mater. Sol. Cells* **2009**, *93*, 851–854. [CrossRef]
5. Battaglia, C.; Erni, L.; Boccard, M.; Barraud, L.; Escarre, J.; Soderstrom, K.; Bugnon, G.; Billet, A.; Ding, L.; Despeisse, M.; et al. Micromorph thin-film silicon solar cells with transparent high-mobility hydrogenated indium oxide front electrodes. *J. Appl. Phys.* **2011**, *109*, 114501. [CrossRef]
6. Jäger, T.; Romanyuk, Y.E.; Bissig, B.; Pianezzi, F.; Nishiwaki, S.; Reinhard, P.; Steinhauser, J.; Schwenk, J.; Tiwari, A.N. Improved open-circuit voltage in Cu(In,Ga)Se_2 solar cells with high work function transparent electrodes. *J. Appl. Phys.* **2015**, *117*, 225303.

7. Jäger, T.; Romanyuk, Y.E.; Nishiwaki, S.; Bissig, B.; Pianezzi, F.; Fuchs, P.; Gretener, C.; Döbeli, M.; Tiwari, A.N. Hydrogenated indium oxide window layers for high-efficiency Cu(In,Ga)Se_2 solar cells. *J. Appl. Phys.* **2015**, *117*, 205301. [CrossRef]
8. Keller, J.; Aijaz, A.; Gustavsson, F.; Kubart, T.; Stolt, L.; Edoff, M.; Törndahl, T. Direct comparison of atomic layer deposition and sputtering of In_2O_3:H used as transparent conductive oxide layer in $CuIn_{1-x}Ga_xSe_2$ thin film solar cells. *Sol. Energy Mater. Sol. Cells* **2016**, *157*, 757–764. [CrossRef]
9. Wardenga, H.F.; Frischbier, M.V.; Morales-Masis, M.; Klein, A. In Situ Hall Effect Monitoring of Vacuum Annealing of In_2O_3:H Thin Films. *Materials* **2015**, *8*, 561–574. [CrossRef]
10. Bielz, T.; Lorenz, H.; Jochum, W.; Kaindl, R.; Klauser, F.; Klötzer, B.; Penner, S. Hydrogen on In_2O_3: Reducibility, Bonding, Defect Formation, and Reactivity. *J. Phys. Chem. C* **2010**, *114*, 9022–9029. [CrossRef]
11. Steigert, A.; Lauermann, I.; Niesen, T.; Dalibor, T.; Palm, J.; Körner, S.; Scherg-Kurmes, H.; Muydinov, R.; Szyszka, B.; Klenk, R. Sputtered Zn(O,S)/In_2O_3:H window layers for enhanced blue response of chalcopyrite solar cells. *Phys. Status Solidi RRL* **2015**, *9*, 627–630. [CrossRef]
12. Dewald, W.; Sittinger, V.; Werner, W.; Jacobs, C.; Szyszka, B. Optimization of process parameters for sputtering of ceramic ZnO:Al_2O_3 targets for a-Si:H/µc-Si:H solar cells. *Thin Solid Films* **2009**, *518*, 1085–1090. [CrossRef]
13. Scherg-Kurmes, H.; Hafez, A.; Siemers, M.; Pflug, A.; Schlatmann, R.; Rech, B.; Szyszka, B. Improvement of the homogeneity of high mobility In_2O_3:H films by sputtering through a mesh electrode studied by Monte Carlo simulation and thin film analysis. *Phys. Status Solidi A* **2016**, *213*, 2310–2316. [CrossRef]
14. Lauermann, I.; Steigert, A. CISSY: A station for preparation and surface/ interface analysis of thin film materials and devices. *J. Large-Scale Res. Fac.* **2016**, *2*, A67. [CrossRef]
15. Storms, H.; Brown, K.; Stein, J. Evaluation of a cesium positive ion source for secondary ion mass spectrometry. *Anal. Chem.* **1977**, *49*, 2023–2030. [CrossRef]
16. Gao, Y. A new secondary ion mass spectrometry technique for III-V semiconductor compounds using the molecular ions CsM^+. *J. Appl. Phys.* **1988**, *64*, 3760–3762. [CrossRef]
17. Magee, C.; Harrington, W.; Botnick, E. On the use of CsX^+ cluster ions for major element depth profiling in secondary ion mass spectrometry. *Int. J. Mass. Spectrom. Ion Process.* **1990**, *103*, 45–56. [CrossRef]
18. Mikami, A. Investigation of $SiCs^+$, $GeCs^+$ and $SiCs_2^+$ Secondary Ion Emission from $Si_{1-x}Ge_x$. *Jpn. J. Appl. Phys.* **2004**, *43*, 2745. [CrossRef]
19. Saha, B.; Chakraborty, P. MCs_n^+-SIMS: An Innovative Approach for Direct Compositional Analysis of Materials without Standards. *Energy Procedia* **2013**, *41*, 80–109. [CrossRef]
20. Odaka, H.; Iwata, S.; Taga, N.; Ohnishi, S.; Kaneta, Y.; Shigesato, Y. Study on electronic structure and optoelectronic properties of indium oxide by first-principles calculation. *Jpn. J. App. Phys.* **1997**, *36*, 5551–5554. [CrossRef]
21. Mryasov, O.N.; Freeman, A.J. Electronic band structure of indium tin oxide and criteria for transparent conducting behaviour. *Phys. Rev. B* **2001**, *64*, 233111. [CrossRef]
22. Robertson, J.; Falabretti, B. *Handbook of Transparent Conductors*; Ginley, D.S., Ed.; Springer Science + Business Media, LLC: Berlin/Heidelberg, Germany, 2010. [CrossRef]
23. Preissler, N.; Bierwagen, O.; Ramu, A.T.; Speck, J.S. Electrical transport, electrothermal transport, and effective electron mass in single-crystalline In_2O_3 films. *Phys. Rev. B* **2013**, *88*, 085305. [CrossRef]
24. Galazka, Z.; Uecker, R.; Irmscher, K.; Schulz, D.; Klimm, D.; Albrecht, M.; Pietsch, M.; Ganschow, S.; Kwasniewski, A.; Fornari, R. Melt growth, characterization and properties of bulk In_2O_3 single crystals. *J. Cryst. Growth* **2013**, *362*, 349–352. [CrossRef]
25. Minami, T.; Kuboi, T.; Miyata, T.; Ohtani, Y. Stability in a high humidity environment of TCO thin films deposited at low temperatures. *Phys. Status Solidi A* **2008**, *205*, 255–260. [CrossRef]
26. Ellmer, K.; Mientus, R. Carrier transport in polycrystalline ITO and ZnO:Al II: The influence of grain barriers and boundaries. *Thin Solid Films* **2008**, *516*, 5829–5835. [CrossRef]
27. Kima, H.-K.; Lee, K.-S. Effect of Introducing H_2O Vapor on Properties of RF Sputter-Grown ITO Anode Layer for OLEDs. *Electrochem. Solid-State Lett.* **2008**, *11*, J57–J59. [CrossRef]
28. Krishnasamy, J.; Chan, K.-Y.; Tou, T.-Y. Influence of process parameters on the substrate heating in direct current plasma magnetron sputtering deposition process. *Microelectron. Int.* **2010**, *27*, 75–78. [CrossRef]
29. Buchholz, D.B.; Ma, Q.; Alducin, D.; Ponce, A.; Jose-Yacaman, M.; Khanal, R.; Medvedeva, J.E.; Chang, R.P.H. The Structure and Properties of Amorphous Indium Oxide. *Chem. Mater.* **2014**, *26*, 5401–5411. [CrossRef]

30. Scherrer, P. Bestimmung der Größe und der inneren Struktur von Kolloidteilchen mittels Röntgenstrahlen. *Göttinger Nachr. Gesell.* **1918**, *2*, 98–100.
31. Genzel, C. X-ray residual stress analysis in thin films under grazing incidence—Basic aspects and applications. *Mater. Sci. Technol.* **2005**, *21*, 10–18. [CrossRef]
32. Bartolomé, J.; Hidalgo, P.; Maestre, D.; Cremades, A.; Piqueras, J. In-Situ Scanning Electron Microscopy and Atomic Force Microscopy Young's Modulus Determination of Indium Oxide Microrods for Micromechanical Resonator Applications. *Appl. Phys. Lett.* **2014**, *104*, 161909. [CrossRef]
33. Zhang, K.H.L.; Regoutz, A.; Palgrave, R.G.; Payne, D.J.; Egdell, R.G. Determination of the Poisson ratio of (001) and (111) oriented thin films of In_2O_3 by synchrotron-based X-ray diffraction. *Phys. Rev. B* **2011**, *84*, 233301. [CrossRef]
34. Remy, H. *Treatise on Inorganic Chemistry: Volume 1*; Elsevier: Amsterdam, The Netherlands, 1956; ISBN 978-0444404701.
35. Egerton, R.F.; Li, P.; Malac, M. Radiation damage in the TEM and SEM. *Micron* **2004**, *35*, 399–409. [CrossRef] [PubMed]
36. Joseph, S.; Berger, S. A study of crystallographic phases in non-stoichiometric (oxygen deficiency) indium oxide thin films. *J. Mater. Sci.* **2017**, *52*, 1988–1995. [CrossRef]
37. Guenther, G.; Schierning, G.; Theissmann, R.; Kruk, R.; Schmechel, R.; Baehtz, C.; Prodi-Schwab, A. Formation of metallic indium-tin phase from indium-tin-oxide nanoparticles under reducing conditions and its influence on the electrical properties. *J. Appl. Phys.* **2008**, *104*, 034501. [CrossRef]
38. Okamoto, H. In-O (Indium-Oxygen). *JPEDAV* **2007**, *28*, 591–592. [CrossRef]
39. Aiyama, T.; Yada, T.J. Plasmon damping in In, Cd and graphite. *J. Phys. Soc. Jpn.* **1975**, *38*, 1357–1361. [CrossRef]
40. Boulenouar, K.; Bouslama, M.; Mokadem, A.; Vizzini, S.; Lounis, Z.; Abdellaoui, A.; Reguad, B.; Bedrouni, M.; Hamaida, K.; Guenouna, T.; et al. Auger Electron Spectroscopy, Electron Energy Loss Spectroscopy, UV Photoelectron Spectroscopy, and Photoluminescence Characterization of In_2O_3 Associated to the Theoretical Calculations Based on the Generalized Gradient Approximation and Modified Becke Johnson. *J. Phys. Chem. C* **2017**, *121*, 8345–8352.
41. Scheel, H.J. *Crystal Growth Technology*; Scheel, H.J., Fukuda, T., Eds.; John Wiley & Sons, Ltd.: Chichester, UK, 2003; 694p, ISBN 0-471-49059-8.
42. Namkoong, G.; Trybus, E.; Lee, K.K.; Moseley, M.; Doolittle, W.A.; Look, D.C. Metal modulation epitaxy growth for extremely high hole concentrations above 10^{19} cm^{-3} in GaN. *Appl. Phys. Lett.* **2008**, *93*, 172112. [CrossRef]
43. Molodyk, A.A.; Korsakov, I.E.; Novojilov, M.A.; Graboy, I.E.; Kaul, A.R.; Wahl, G. Volatile Surfactant-Assisted MOCVD: Application to $LaAlO_3$ Thin-Film Growth. *Chem. Vapor Depos.* **2000**, *6*, 133–138. [CrossRef]
44. Koida, T.; Kondo, M.; Tsutsumi, K.; Sakaguchi, A.; Suzuki, M.; Fujiwara, H. Hydrogen-Doped In_2O_3 Transparent Conducting Oxide Films Prepared By Solid-Phase Crystallization Method. *J. Appl. Phys.* **2010**, *107*, 033514. [CrossRef]
45. Macco, B.; Knoops, H.C.M.; Kessels, W.M.M. Electron Scattering and Doping Mechanisms in Solid-PhaseCrystallized In_2O_3:H Prepared by Atomic Layer Deposition. *ACS Appl. Mater. Interfaces* **2015**, *7*, 16723–16729. [CrossRef] [PubMed]
46. Muranaka, S.; Bando, Y.; Takada, T. Influence of substrate temperature and film thickness on the structure of reactively evaporated In_2O_3 films. *Thin Solid Films* **1987**, *151*, 355–364. [CrossRef]
47. Pflug, A.; Sittinger, V.; Ruske, F.; Szyszka, B.; Dittmar, G. Optical characterization of aluminum-doped zinc oxide films by advanced dispersion theories. *Thin Solid Films* **2004**, *455–456*, 201–206. [CrossRef]
48. Wirtz, G.P.; Takiar, H.P. Oxygen Diffusion in Vapor-Deposited Indium Oxide Films. *J. Am. Ceram. Soc.* **1981**, *64/12*, 748–752. [CrossRef]
49. Pan, C.A.; Ma, T.P. Work function of In_2O_3 film as determined from internal photoemission. *Appl. Phys. Lett.* **1980**, *37*, 714–716. [CrossRef]
50. Hohmann, M.V.; Ágoston, P.; Wachau, A.; Bayer, T.J.; Brötz, J.; Albe, K.; Klein, A. Orientation dependent ionization potential of In_2O_3: A natural source for inhomogeneous barrier formation at electrode interfaces in organic electronics. *J. Phys. Condens. Matter* **2011**, *23*, 334203. [CrossRef]
51. Shaker, A.; Zekry, A. A New and Simple Model for Plasma-and Doping-Induced Band Gap Narrowing. *J. Electron Devices* **2010**, *8*, 293–299.

52. Jia, J.; Oka, N.; Shigesato, Y. Direct observation of the band gap shrinkage in amorphous In_2O_3–ZnO thin films. *J. Appl. Phys.* **2013**, *113*, 163702. [CrossRef]
53. Vanýsek, P. *Handbook of Chemistry and Physics*, 81th ed.; Electrochemical Series; CRC Press LLC: Boca Raton, FL, USA, 2000; ISBN 978-0849304811.
54. Schoeller, H.E. Thermodynamics and Kinetics of Oxidation and Temperature Dependent Mechanical Characterization of Pure Indium Solder. Ph.D. Thesis, State University of New York, Binghamton, NY, USA, 2007; UMI Number: 1447566.
55. Mukhopadhyay, S.; Gowtham, S.; Pandey, R.; Costales, A. Theoretical study of small clusters of indium oxide: InO, In_2O, InO_2, In_2O_2. *J. Mol. Struct. THEOCHEM* **2010**, *948*, 31–35. [CrossRef]
56. Gordon, D.F.; Helle, M.H.; Jones, T.G.; Fung, K. *CHMWTR: A Plasma Chemistry Code for Water Vapor*; NRL/MR/6790-12-9383; Naval Research Laboratory Report: Washington, WA, USA, 2011.
57. Coburn, J.W.; Taglauer, E.; Kay, E. A study of the neutral species rf-sputtered from oxide targets. *Jpn. J. Appl. Phys. Suppl.* **1974**, *2*, 501–504. [CrossRef]
58. Snyder, D.; Carmichael, I.S.E. Olivine-liquid equilibria and the chemical activities of FeO, NiO, Fe_2O_3, and MgO in natural basic melts. *Geochim. Cosmochim. Acta* **1991**, *56*, 303–318. [CrossRef]
59. Chatterji, D.; Vest, R.W. Thermodynamic Properties of the System Indium-Oxygen. *J. Am. Ceram. Soc.* **1972**, *55*, 575–578. [CrossRef]
60. Coburn, J.W.; Kay, E. Positive-ion bombardment of substrates in rf diode glow discharge sputtering. *J. Appl. Phys.* **1972**, *43*, 4965–4971. [CrossRef]
61. Tominaga, K.; Sueyoshi, Y.; Munfei, Ch.; Chintani, Y. Energetic O^- ions and O atoms in planar magnetron sputtering of ZnO target. *Jpn. J. Appl. Phys.* **1993**, *32*, 4131–4135. [CrossRef]
62. Pierre, A.C. Gelation of Aluminum Hydroxide Sols. *J. Am. Ceram. Soc.* **1987**, *70*, 28–32. [CrossRef]
63. Koga, N.; Kimizu, T. Thermal Decomposition of Indium (III) Hydroxide Prepared by the Microwave-Assisted Hydrothermal Method. *J. Am. Ceram. Soc.* **2008**, *91*, 4052–4058. [CrossRef]
64. Jost, G.C.E.; Hamri, A.N.; Köhler, F.; Hüpkes, J. Reliability aspects of hydrogen-doped indium oxide. *Phys. Status Solidi A* **2016**, *213*, 1751–1759. [CrossRef]
65. Sudakar, C.; Dixit, A.; Kumar, S.; Sahana, M.B.; Lawes, G.; Naika, R.; Naik, V.M. Coexistence of anion and cation vacancy defects in vacuum-annealed In_2O_3 thin films. *Scr. Mater.* **2010**, *62*, 63–66. [CrossRef]
66. King, P.D.C.; Lichti, R.L.; Celebi, Y.G.; Gil, J.M.; Vilão, R.C.; Alberto, H.V.; Duarte, J.P.; Payne, D.J.; Egdell, R.G.; McKenzie, I.; et al. Shallow donor state of hydrogen in In_2O_3 and SnO_2: Implications for conductivity in transparent conducting oxides. *Phys. Rev. B* **2009**, *80*, 081201(R). [CrossRef]
67. Agoston, P.; Albe, K.; Nieminen, R.M.; Puska, M.J. Intrinsic n-type behavior in transparent conducting oxides: A comparative hybrid-functional study of In_2O_3, SnO_2, and ZnO. *Phys. Rev. Lett.* **2009**, *103*, 245501. [CrossRef] [PubMed]
68. De Wit, J.H.W. Structural Aspects and Defect Chemistry in In_2O_3. *J. Sol. St. Chem.* **1977**, *20*, 143–148. [CrossRef]
69. Liu, J.; Liu, T.; Liu, F.; Li, H. Thermodynamics of native defects in In_2O_3 crystals using a first-principles method. *RSC Adv.* **2014**, *4*, 36983–36989. [CrossRef]
70. Reunchan, P.; Zhou, X.; Limpijumnong, S.; Janotti, A.; Van de Walle, C.G. Vacancy defects in indium oxide: An ab-initio study. *Curr. Appl. Phys.* **2011**, *11*, S296–S300. [CrossRef]
71. Limpijumnong, S.; Reunchan, P.; Janotti, A.; Van de Walle, C.G. Hydrogen doping in indium oxide: An *ab initio* study. *Phys. Rev. B* **2009**, *80*, 193202. [CrossRef]
72. Tomita, T.; Yamashita, K.; Hayafuji, Y. The origin of *n*-type conductivity in un-doped In_2O_3. *Appl. Phys. Lett.* **2005**, *87*, 051911. [CrossRef]
73. Shannon, R.D. Revised Effective Ionic Radii and Systematic Studies of Interatomie Distances in Halides and Chaleogenides. *Acta Cryst. A* **1976**, *32*, 751–767. [CrossRef]
74. Bushema, I.S.; Headridge, J.B. Determination of indium by hydride generation and atomic-absorption spectrometry. *Talanta* **1982**, *29*, 519–520. [CrossRef]
75. Raghavachari, K.; Fu, Q.; Chen, G.; Li, L.; Li, C.H.; Law, D.C.; Hicks, R.F. Hydrogen Adsorption on the Indium-Rich Indium Phosphide (001) Surface: A Novel Way to Produce Bridging In-H-In Bonds. *J. Am. Chem. Soc.* **2002**, *124*, 15119–15124. [CrossRef]

76. Lany, S.; Zunger, A. Comment on "Intrinsic n-type Behavior in Transparent Conducting Oxides: A Comparative Hybrid-Functional Study of In_2O_3, SnO_2, and ZnO". *Phys. Rev. Lett.* **2011**, *106*, 069601. [CrossRef]
77. Ohya, Y.; Yamamoto, T.; Ban, T. Equilibrium Dependence of the Conductivity of Pure and Tin-Doped Indium Oxide on Oxygen Partial Pressure and Formation of an Intrinsic Defect Cluster. *J. Am. Ceram. Soc.* **2008**, *91*, 240–245. [CrossRef]
78. Szczyrbowski, J.; Dietrich, A.; Hoffmann, H. Optical Properties of RF-Sputtered Indium Oxide Films. *Phys. Stat. Sol. A* **1982**, *69*, 217–226. [CrossRef]
79. Ibragimov, Kh.I.; Korol'kov, V.A. Temperature Dependence of the Work Function of Metals and Binary Alloys. *Inorg. Mater.* **2001**, *37*, 567–572. [CrossRef]
80. Claflin, B.; Fritzsche, H. The Role of Oxygen Diffusion in Photoinduced Changes of the Electronic and Optical Properties in Amorphous Indium Oxide. *J. Electron. Mater.* **1996**, *25*, 1772–1777. [CrossRef]
81. Guilmeau, E.; Berardan, D.; Simon, C.; Maignan, A.; Raveau, B.; Ovono, D.O.; Delorme, F. Tuning the transport and thermoelectric properties of In_2O_3 bulk ceramics through doping at In-site. *J. Appl. Phys.* **2009**, *106*, 053715. [CrossRef]